PAPER

NSTX/NSTX-U theory, modeling and analysis results

IOP Publishing | International Atomic Energy Agency Nuclear Fusion

Nucl. Fusion **59** (2019) 112007 (16pp) https://doi.org/10.1088/1741-4326/ab023a

NSTX/NSTX-U theory, modeling and analysis results

S.M. Kaye[1], D.J. Battaglia[1], D. Baver[2], E. Belova[1], J.W. Berkery[3], V.N. Duarte[1], N. Ferraro[1], E. Fredrickson[1], N. Gorelenkov[1], W. Guttenfelder[1], G.Z. Hao[4], W. Heidbrink[4], O. Izacard[5], D. Kim[1], I. Krebs[1], R. La Haye[6], J. Lestz[1], D. Liu[4], L.A. Morton[7], J. Myra[2], D. Pfefferle[1], M. Podesta[1], Y. Ren[1], J. Riquezes[3], S.A. Sabbagh[3], M. Schneller[1], F. Scotti[8], V. Soukhanovskii[8], S.J. Zweben[1], J.W. Ahn[9], J.P. Allain[10], R. Barchfeld[11], F. Bedoya[12], R.E. Bell[1], N. Bertelli[1], A. Bhattacharjee[1], M.D. Boyer[1], D. Brennan[5], G. Canal[13], J. Canik[9], N. Crocker[14], D. Darrow[1], L. Delgado-Aparicio[1], A. Diallo[1], C. Domier[11], F. Ebrahimi[1], T. Evans[6], R. Fonck[7], H. Frerichs[7], K. Gan[15], S. Gerhardt[1], T. Gray[9], T. Jarboe[16], S. Jardin[1], M.A. Jaworski[1], R. Kaita[1], B. Koel[5], E. Kolemen[5], D.M. Kriete[7], S. Kubota[14], B.P. LeBlanc[1], F. Levinton[17], N. Luhmann[11], R. Lunsford[1], R. Maingi[1], R. Maqueda[18], J.E. Menard[1], D. Mueller[1], C.E. Myers[19], M. Ono[1], J.-K. Park[1], R. Perkins[1], F. Poli[1], R. Raman[16], M. Reinke[9], T. Rhodes[14], C. Rowley[5], D. Russell[2], E. Schuster[20], O. Schmitz[7], Y. Sechrest[17], C.H. Skinner[1], D.R. Smith[7], T. Stotzfus-Dueck[1], B. Stratton[1], G. Taylor[1], K. Tritz[21], W. Wang[1], Z. Wang[1], I. Waters[7] and B. Wirth[15]

[1] Princeton Plasma Physics Laboratory, Princeton University, Princeton, NJ 08543, United States of America
[2] Lodestar Research Corporation, Boulder, CO, United States of America
[3] Columbia University, New York, NY, United States of America
[4] University of California at Irvine, Irvine, CA, United States of America
[5] Princeton University, Princeton, NJ, United States of America
[6] General Atomics, San Diego, CA, United States of America
[7] University of Wisconsin, Madison, WI, United States of America
[8] Lawrence Livermore National Laboratory, Livermore, CA, United States of America
[9] Oak Ridge National Laboratory, Oak Ridge, TN 37831, United States of America
[10] University of Illinois at Urbana-Champaign, Urbana, IL, United States of America
[11] University of California at Davis, Davis, CA, United States of America
[12] Massachusetts Institute of Technology, Cambridge, MA, United States of America
[13] Institute of Physics, University of Sao Paolo, Sao Paolo, Brazil
[14] University of California at Los Angeles, Los Angeles, CA, United States of America
[15] University of Tennessee, Knoxville, TN, United States of America
[16] University of Washington, Seattle, WA, United States of America
[17] Nova Photonics, Princeton, NJ, United States of America
[18] X Science LLC, Plainsboro, NJ, United States of America
[19] Los Alamos National Laboratory, Los Alamos, NM, United States of America
[20] Lehigh University, Bethlehem, PA, United States of America
[21] Johns Hopkins University, Baltimore, MD, United States of America

E-mail: kaye@pppl.gov

Received 30 November 2018, revised 14 January 2019
Accepted for publication 28 January 2019
Published 5 June 2019

Abstract

The mission of the spherical tokamak NSTX-U is to explore the physics that drives core and pedestal transport and stability at high-β and low collisionality, as part of the development of the spherical tokamak (ST) concept towards a compact, low-cost ST-based pilot plant. NSTX-U will ultimately operate at up to 2 MA and 1 T with up to 12 MW of neutral beam injection power for 5 s. NSTX-U will operate in a regime where electromagnetic instabilities are expected to dominate transport, and beam-heated NSTX-U plasmas will explore a portion of energetic particle parameter space that is relevant for both α-heated conventional and low aspect ratio burning plasmas. NSTX-U will also develop the physics understanding and control tools to ramp-up and sustain high performance plasmas in a fully-noninductive fashion. NSTX-U began research operations in 2016, but a failure of a divertor magnetic field coil after ten weeks of operation resulted in the suspension of operations and initiation of recovery activities. During this period, there has been considerable work in the area of analysis, theory and modeling of data from both NSTX and NSTX-U, with a goal of understanding the underlying physics to develop predictive models that can be used for high-confidence projections for both ST and higher aspect ratio regimes. These studies have addressed issues in thermal plasma transport, macrostability, energetic particlet-driven instabilities at ion-cyclotron frequencies and below, and edge and divertor physics.

Keywords: NSTX, NSTX-U, overview

(Some figures may appear in colour only in the online journal)

1. Introduction

The mission of the spherical tokamak NSTX-U [1] is to explore the physics that drives core and pedestal transport and stability at high-β and low collisionality, as part of the development of the spherical tokamak (ST) concept towards a compact, low-cost ST-based pilot plant [2–4]. NSTX-U will operate at up to 2 MA and 1 T with up to 12 MW of neutral beam injection (NBI) power for 5 s. NSTX-U will study electromagnetic instabilities, which are expected to dominate transport in the core and a portion of neutral beam-energetic particle (EP) phase space that is relevant for both α-heated conventional and low aspect ratio burning plasmas. At high-β, virulent non-linear EP-driven instabilities are expected to occur, and NSTX-U will be developing means to suppress or mitigate the modes through tailored NB injection and to develop models to predict the enhanced EP transport caused by these modes. NSTX-U will also develop the physics understanding and control tools to ramp-up and sustain high performance plasmas in a fully-non-inductive regime, aided by the flexible aiming of the NBI-system for current and rotation control.

In particular, NSTX-U will be addressing issues critical to developing the basis for, and optimizing the design of, an ST configuration-based pilot plant, which has a goal of a non-inductively sustained, net electricity producing plasma. Critical issues include identifying and developing a capability to predict transport and confinement across a range of normalized collisionality ($\nu_* = \nu/a$) and normalized gyroradius ($\rho_* = \rho/a$). Developing this predictive capability requires the same for the energetic particle population, a source of heating and non-inductive current drive. Fusion power production is proportional to β^4 for a given toroidal magnetic field [3, 4], and maximizing β requires understanding magnetohydrodynamic (MHD) stability limits, the development of predictive algorithms for disruption avoidance through real-time control actuators, and understanding the effect of disruptions, if they cannot be avoided, on material surfaces. The sustainment of discharges requires knowledge of processes that can influence the flow of heat to first walls and divertor regions, and developing approaches to mitigating these heat loads. It is the synthesis of understanding in all these areas that is needed for developing optimized designs, with respect to and among other things, aspect ratio, toroidal magnetic field and plasma shaping for an ST pilot plant.

NSTX-U began research operations in 2016, producing 10 weeks of commissioning and scientific results [5, 6]. However, a number of technical issues, including the failure of a key divertor magnetic field coil, resulted in the suspension of operations and initiation of recovery activities. During this period, there has been considerable work in the area of analysis, theory and modeling of data from both NSTX and NSTX-U, with a goal of understanding the underlying physics to develop predictive models that can be used for projections for both ST and higher aspect ratio regimes. This paper will discuss results of these studies in the areas of confinement and transport, macrostability, energetic particle physics, and edge and divertor physics.

2. Transport and confinement

2.1. Gyrokinetic analysis of L-mode plasmas

Low confinement (L-) mode transport modeling has been revisited in light of recent research that has illustrated the importance of cross-scale coupling between ion- and electron-scale turbulence [7–9]. Local nonlinear gyrokinetic simulations run

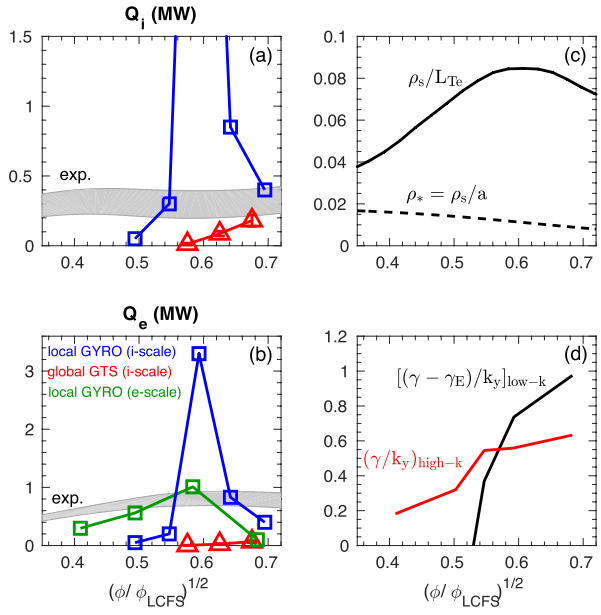

Figure 1. Comparison of simulated and experimentally inferred (*a*) ion and (*b*) electron thermal heat fluxes. (*c*) Profile of local parameters, $\rho_* = \rho_s/a$, and ρ_s/L_{Te}. (*d*) Ratio of gyro-Bohm normalized growth rate to poloidal wavenumber for maximum growth rate for ion scale ($k_y = k_\theta \rho_s < 1$) and electron scale ($k_y = k_\theta \rho_s > 1$).

for an NSTX L-mode [10] predicted ion-scale transport that peaked at very large values around $\rho \simeq r/a = 0.6$ (figures 1(*a*) and (*b*)). However, there is a rapid reduction in transport on either side of this peak due to (i) $E \times B$ shearing rates becoming larger than linear growth rates towards the core, and (ii) a reduction in the gyro-Bohm coefficient $Q_{GB} \sim T^{5/2}$ towards the edge. Global nonlinear ion scale simulations using GTS [11, 12] predict a much smoother variation of transport as a consequence of profile shearing effects at the relatively large values of $\rho^* = \rho_s/a$ (or ρ_s/L_{Te}) (figure 1(*c*)). The global simulations reproduce ion thermal transport comparable to experiment when neoclassical transport is added to the calculated turbulent transport. However, predicted electron heat flux in the global simulations is negligible indicating that some physics is still missing.

Linear analysis predicts electron temperature gradient (ETG) modes to also be unstable, and local, nonlinear ETG simulations in the same region using numerical grids that resolve only electron-scale turbulence $[L_x, L_y] = [6, 4]\rho_s = [360, 240]\rho_e$, $[nx, ny] = [192, 48]$ have been run [13, 14]. As seen in figure 1(*b*), the ETG simulations predict significant transport around the mid-radius, approaching experimental levels. Given the similarity in electron heat flux at electron scales and ion heat flux at ion scales from simulations ($Q_{e,high-k} \simeq Q_{i,low-k}$), cross-scale coupling effects cannot be ruled out. The potential importance of multi-scale effects is further supported by noting that the ratio of the maximum γ/k_y (growth rate/wave number) predicted from the electron-scale instability is comparable to or exceeds that predicted for the ion-scale instability (figure 1(*d*)). This metric

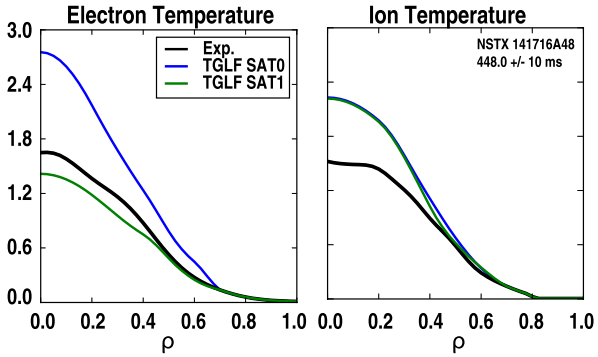

Figure 2. Comparison of measured and predicted T_e and T_i profiles for an NSTX L-mode plasma. The predicted profiles use the TGLF model with two different saturation models.

has been proposed as a criterion for indicating the potential importance of multi-scale effects [9].

Profile predictions for this L-mode discharge using the reduced model TGLF [15] have also been validated against measured profiles. Figure 2 shows the predicted T_e and T_i profiles for the original saturation model 'SAT0' significantly overpredict the temperatures. However, using the recently updated 'SAT1' saturation model that accounts for cross-scale coupling [16] provides an increase in electron thermal transport that brings the predicted profiles into much better agreement with experiment. The agreement between the TGLF-SAT1 predictions and experiment lend additional motivation to pursue full multi-scale gyrokinetic simulation (that simultaneously simulate ion-to-electron scales) to directly predict the importance of cross-scale coupling. We note, however, that TGLF is a local model, and given the obvious impact of non-local effects on the ion-scale turbulence predicted in the gyrokinetic simulations (figure 2(*a*)) it is possible that a combination of global plus multiscale would be required to predict the complete ion and electron thermal transport profiles. (Similar implications are found for both NSTX-U L-modes [16] and recent NSTX H-mode analysis [17].) The feasibility of such simulations is unclear and will require careful future exploration as computational resources increase. We also note that TGLF simulations with either saturation rule have not been successful to-date in predicting H-mode T_e profiles that agree with experimental observations. Further development of the model for applicability in low aspect ratio, high-β regimes is required.

2.2. L-H and EPH-mode physics

Resilience to vertical displacement events (VDEs) at higher shaping ($\kappa > 2.5$) on NSTX and NSTX-U improved with a broader current profile (low l_i), and triggering the H-mode early in the I_p ramp ($I_p < 0.5$ MA) slows the penetration of the current to the core and enables low-l_i operation, where l_i is a measure of plasma inductance, and low l_i plasmas have broad plasma current profiles. A database of 68 diverted discharges from the 2016 operation of NSTX-U was used to identify the target conditions for reliable H-mode access during ramp-up

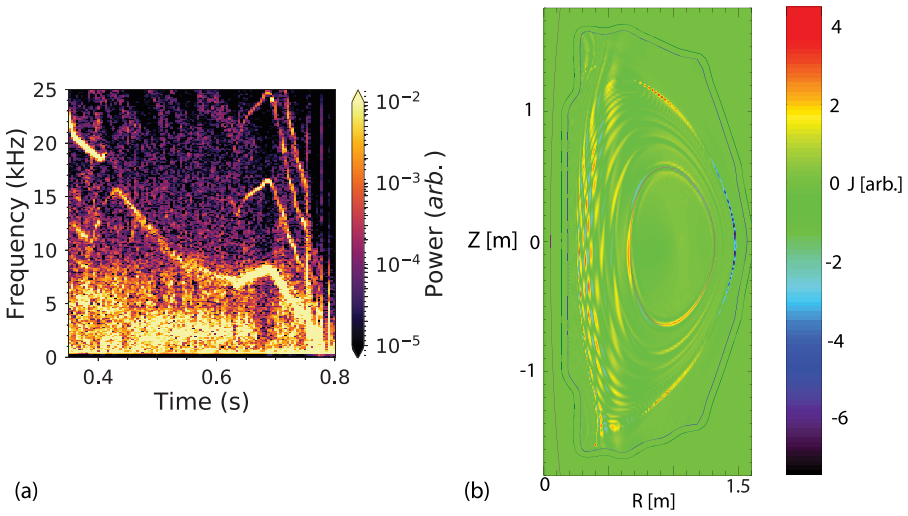

Figure 3. (*a*) Spectrogram of $n = 1$ magnetic amplitude for 2/1 mode from NSTX discharge 134020, (*b*) mode structure from M3D-C1 linear simulation at $t = 627$ ms for mode in (*a*).

when using 3–5 MW of NBI heating. The set of criteria that were identified included: line-averaged density exceeding 1.25×10^{19} m^{-3}, surface voltage of the plasma <1.15 V, shape close to double null, and oxygen content below a critical threshold. The results suggest it is unlikely to trigger an L–H transition with only two criteria met but very likely when satisfying all four. Other criteria, such as I_p and dI_p/dt, were considered, but were found to be not as important as the four mentioned above. These results can influence the development of the target boundary shape, neutral fueling and loop voltage evolution during operations, and can lead to reliable triggering of the L–H transition early in the I_p ramp.

The enhanced pedestal H (EPH)-mode [18] features the development of a wider H-mode pedestal with a significant increase in the ion temperature and carbon rotation gradients in an edge localized mode (ELM)- and MHD-free period following a large ELM. These discharges achieve improved energy and momentum confinement with a beneficial decrease in the impurity accumulation relative to a standard ELM-free H-mode regime. Recent analysis of EPH-mode discharges demonstrates that the transport bifurcation is triggered by a transient period of lower collisionality during the ELM recovery where the ∇T_i increases consistent with neoclassical ion thermal transport. The transient period of larger ∇T_i reinforces the lower edge collisionality via a reduction of the neoclassical impurity pinch and movement of the region of large E_r shearing rate toward the core. These effects lead to a wider density pedestal providing access to larger pedestal pressures that are stable to peeling instabilities. The larger ∇T_i also acts to stabilize electron-scale turbulence, improving the edge electron thermal barrier. The favorable positive feedback in the pedestal structure that is initiated by transiently accessing lower edge ion collisionality motivates the continued focus on developing actuators for controlling the edge pedestal collisionality that are compatible with large core density and heat flux mitigation on NSTX-U.

3. Macrostability

3.1. Neoclassical tearing modes (NTMs)

Tearing-type modes with $n = 1$, $m = 2$ helicity have been observed on both NSTX and NSTX-U. As observed on NSTX, soft x-ray measurements indicate coupling to a core-localized $n = 1$, $m = 1$ perturbation, leading to flattening of the rotation profile from the core to the $q = 2$ surface [19, 20]. In the discharges studied, the magnetic mode amplitude grew smoothly from the Mirnov array noise floor island width, which is comparable to the ion gyro-radius. The gradual mode onset is indicative of a so-called 'spontaneous' mode [21], as opposed to the paradigmatic NTM onset [22] in which the mode is metastable and is triggered instantaneously at finite amplitude by an exogenous magnetic perturbation. Prior to the emergence of the mode amplitude definitively above the noise floor, a faint precursor fluctuation is seen in many cases (figure 3(*a*), $t < 0.6$ s). It is not yet clear whether this represents turbulent excitation of a marginally-stable mode, or a mode that is linearly unstable but saturated at very low amplitude. The physics of the tearing mode in the small-island regime (width comparable to ion gyro-radius and consequently to drift wave turbulence scales) is still uncertain, with many possible effects at play [23]. Similar $n = 1$ tearing mode behavior is observed in NSTX-U plasmas with higher B_T, more neutral beam heating power for similar high normalized β, and higher T_e for a longer resistive diffusion time.

Linear M3D-C1 [24] simulations indicate an instability, which comprises multiple poloidal harmonics and which is consistent with strong toroidicity-induced coupling at low aspect ratio (figure 3(*b*)). In these simulations, the mode is suppressed by inclusion of the measured plasma rotation profile, presumably due to shear. Resistive DCON stability calculations yield positive tearing stability index well before and during the mode onset in all discharges studied. The stabilizing Glasser–Green–Johnson (GGJ) effect (due to field line

curvature and pressure gradient) is thought to counteract the destabilizion. The GGJ effect increases at lower aspect ratio R/a, and is therefore expected to be more advantageously significant in NSTX/NSTX-U than standard-aspect tokamaks such as DIII-D [25]. However, the expansion of the center column in NSTX-U should weaken this stabilizing effect over that in NSTX; dedicated experiments in NSTX-U are needed to confirm this.

3.2. Disruption prediction, avoidance and mitigation

DECAF [26, 27] code development has now produced significantly increased capability by automatically identifying rotating MHD instabilities, their bifurcation, and locking. The toroidal mode number is now also automatically determined for an arbitrary number of modes occurring simultaneously. The capability has been generalized to operate on any tokamak data available to DECAF. The information analyzed for these modes along with plasma rotation profile and other plasma measurements (15 criteria presently used for analysis of NSTX) produces predictive warning signals for the modes, along with a total MHD event warning signal showing initial success as a disruption forecaster. These capabilities are illustrated for an NSTX disruption in figure 4. In the shot analyzed, rotating MHD instabilities thought to be non-linearly saturated and slowly evolving resistive modes are found by a generalized phase matching algorithm in DECAF using an array of toroidal magnetic probes. The code discriminates the toroidal mode number, n, of the instabilities and tracks all modes greater than a specified amplitude, including modes that occur simultaneously. A single total MHD warning signal that depends on up to 15 separate criteria, and that varies with time, is also shown. A significant part of DECAF analysis is determining the best sets of criteria to choose to create a predictive DECAF warning signal. For the present model, a total warning level of 4 indicates close proximity to the disruption. The algorithm also gives us an understanding of what is happening in the plasma to create dangerous plasma states approaching the disruption. For example, early in the discharge, MHD modes are found, and core plasma rotation is low as the plasma starts up and typically transitions from counter-NBI rotation to co-NBI rotation. The mode frequencies are relatively high at this time, which is generally a safe condition. Later, near $t = 0.25$ s, the MHD warning level increases as modes are found with decreased and decreasing rotation frequency. However, these frequencies are not critically low (no mode bifurcations are found) and plasma rotation is not low, so the warning level remains low. However, later on, more negative criteria occur simultaneously, including increased mode amplitude, decreasing mode frequencies and decreasing plasma rotation across the profile. Close to the time of the disruption, the modes drop to a very low frequency, and core plasma rotation is low, leading to model locking and growth toward a critical level of locked mode amplitude. DECAF starts to show a significant change in the MHD warning level about 200 ms earlier than this, providing advanced notice of the potential disruption.

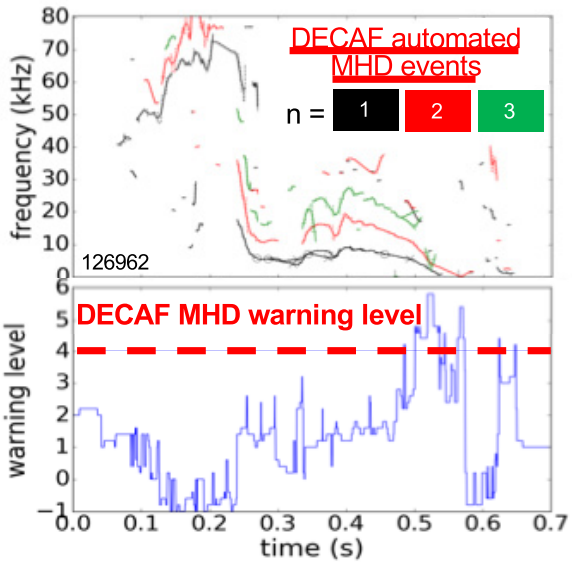

Figure 4. DECAF decomposition of rotating MHD in a relatively slow evolution toward disruption.

3.3. Vertical displacement event (VDE) modeling

Three-dimensional (3D) simulations of a vertically unstable NSTX discharge were carried out using M3D-C1 in order to investigate the formation of non-axisymmetric halo currents during a nominally axisymmetric event [28]. This work was also intended to inform the development of future halo current diagnostics on NSTX-U. These simulations were initialized with a vertically unstable equilibrium reconstruction of an NSTX discharge. In both the discharge and the simulation, the plasma control system was disabled to observe the evolution of the VDE under the condition of fixed coil currents. Disruption mitigation was not applied, so the plasma remained hot and essentially axisymmetric as it drifted vertically toward the wall.

In the simulation, the plasma remained stable to non-axisymmetric modes until well after it made contact with the wall. Once contact was made, the edge plasma was scraped off while the core plasma remained hot. While the low resistivity in the core caused the safety factor profile there to remain fixed, the contraction of the plasma current due to the scraping-off gave rise to strong skin currents at the edge that eventually become unstable, first at moderate toroidal mode numbers ($n \sim 5$), and then at lower toroidal mode numbers. The non-axisymmetric halo currents due to these instabilities showed a similar pattern of forming first at moderate n and then coalescing to lower n. These instabilities stochasticize the edge, leading to a fast thermal quench due to parallel heat losses. Figure 5 shows the evolution of the VDE, halo current generation and resulting $j \times B$ forces on the wall.

Axisymmetric M3D-C1 simulations were also carried out for an NSTX-U model equilibrium with $I_p = 2$ MA in order to assess forces on coils during VDEs. These calculations were initialized with a vertically unstable model NSTX-U equilibrium. Two cases were considered: one with a drift time

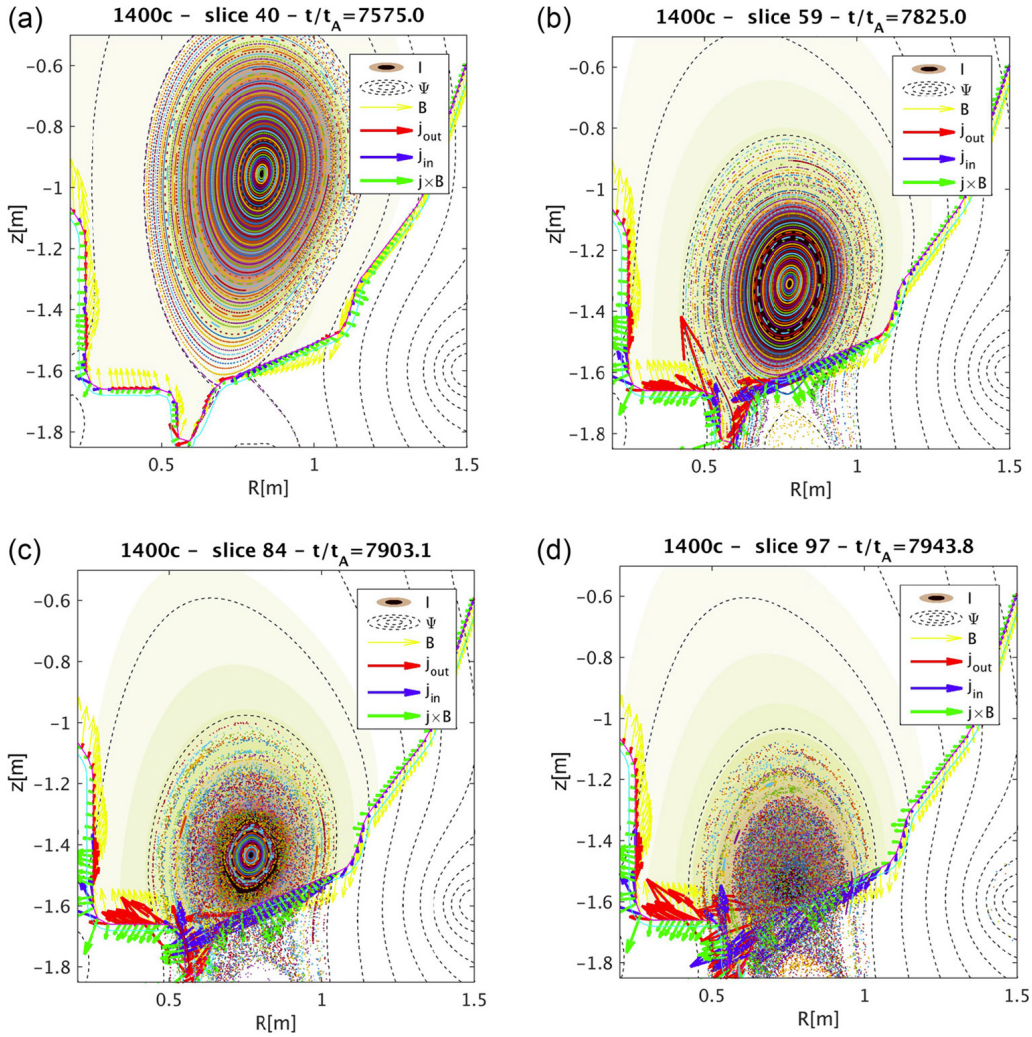

Figure 5. Poincaré plots at a sequence of times in a 3D M3D-C1 simulation an actual NSTX discharge that went vertically unstable. Red and blue arrows show halo currents into and out of the wall, respectively. Green arrows show the direction of the poloidal electromagnetic force density on the wall. Reprinted from [28], with the permission of AIP Publishing.

of ∼10 ms, and the other with a drift time of ∼20 ms. The drift time was changed by scaling the resistivity of the wall in M3D-C1. The ensuing VDE was simulated without introducing any disruption mitigation, in order to present a 'worst-case' scenario. The thermal energy and toroidal current are plotted as a function of time for these simulations in figure 6.

It was found that the VDE generated excess radial field at on the order of 0.1 T for coils in the polar region towards which the plasma displaces. The maximum excess field in these simulations was found to be largely independent of the drift time for the cases considered; therefore, the expected impulse to each coil is expected to scale approximately linearly with the drift time, if the coil currents were held fixed over this time. In reality, the drift times considered here significantly exceed the current ramp-down time of the coils, and therefore ramping down the coil currents at the onset of the disruption is expected to be an effective measure for avoiding sudden forces during these events.

4. Energetic particle physics

4.1. Fast ion redistribution by sawteeth

In the NSTX-U 2016 campaign, 2 s long L-mode sawtoothing discharges were routinely achieved, providing an opportunity to study the effects of sawteeth on fast ion transport in STs. Repetitive drops in neutron rate accompanied by increases of edge D_α emission were observed at each sawtooth event (figure 7(*b*)), suggesting that fast ions were lost or redistributed, in addition to the redistribution of thermal plasma as a result of the flux reconnection. The solid-state neutral particle analyzer (SSNPA) and fast ion D_α (FIDA) diagnostics are used to infer fast ion transport by sawteeth. Both systems have a tangentially-viewing instrument and a radially- or vertically-viewing instrument, which are mainly sensitive to passing and trapped fast ions, respectively. It has been observed on both diagnostics that passing particles were strongly expelled from the plasma core

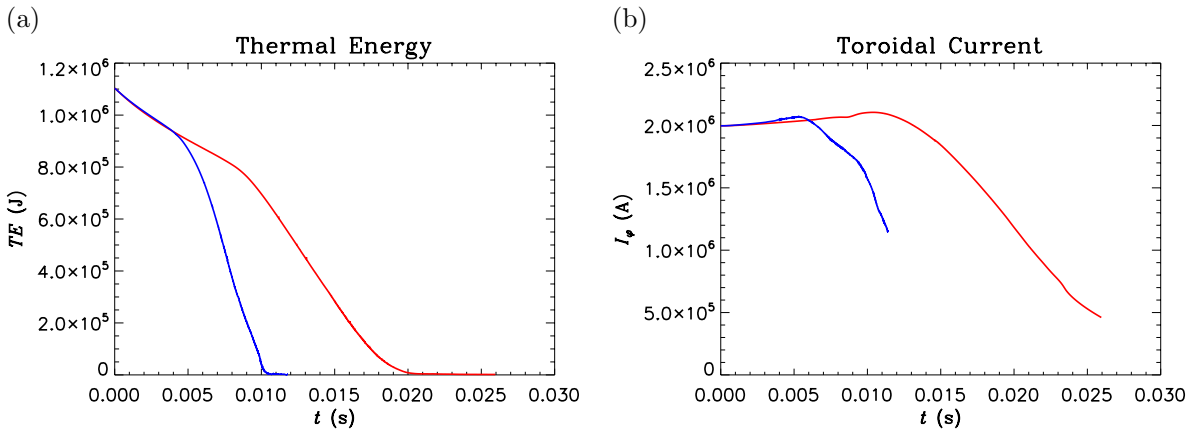

Figure 6. The thermal energy (left) and the toroidal current (right) from 2D M3D-C1 simulations of a vertical displacement event in NSTX-U model discharge. The simulations were performed to explore the effect of the current quench time on the wall and coil forces. Blue and red lines show cases in which the drift time is ∼10 ms and ∼20 ms, respectively.

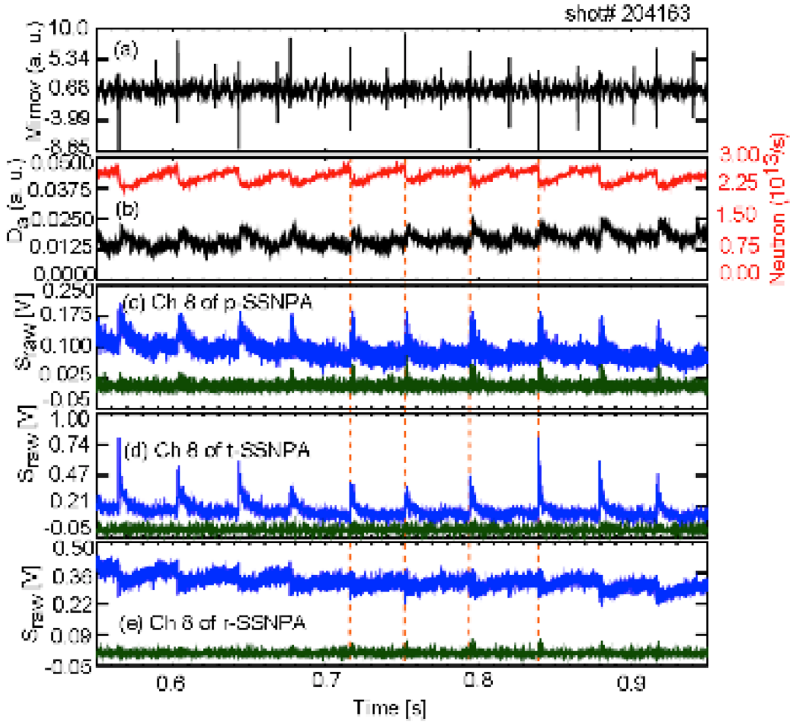

Figure 7. Temporal evolution of (*a*) Mirnov coil signals, (*b*) neutron emission and D_α radiance from the edge of the plasma, (*c*) signal of passive-SSNPA, (*d*) signal of tangentially-viewing SSNPA and (*e*) signal of radially-viewing SSNPA. Reproduced courtesy of IAEA. Figure from [29]. Copyright 2018 IAEA.

to the edge during sawtooth crashes, while trapped fast ions were weakly affected [29]. The tangentially-viewing SSNPA, which is mainly sensitive to passing fast ions, observed large signal spikes at the sawtooth crashes (figure 7(*d*)) because fast ions moved to the edge and charge exchanged with edge neutrals. The radially-viewing SSNPA data suggest that there was a small drop of trapped particles in the core (figure 7(*e*)). The tangentially-viewing FIDA (t-FIDA) system, which is sensitive to passing fast ions, observed a depletion as large as 25% inside the inversion radius, but an increase at the outer region (figure 8(*d*)). Within the experimental uncertainties, there is almost no change in the signals of the vertically-viewing FIDA system.

TRANSP simulations with the Kadomstev and Porcelli sawtooth models were performed. While the Kadomtsev model, which assumes full reconnection of the flux inside the $q = 1$ surface, overestimates the neutron rate drop at each sawtooth event, the partial reconnection Porcelli model qualitatively reproduced the neutron rate drop when tuning the sawtooth model parameters. However, both sawtooth models cannot fully reproduce the observations of the t-FIDA signal change. The discrepancy suggests that the models presently implemented in TRANSP may be too simple to capture details of the variation of the fast ion distribution induced by sawteeth. In particular, introducing phase space selectivity for

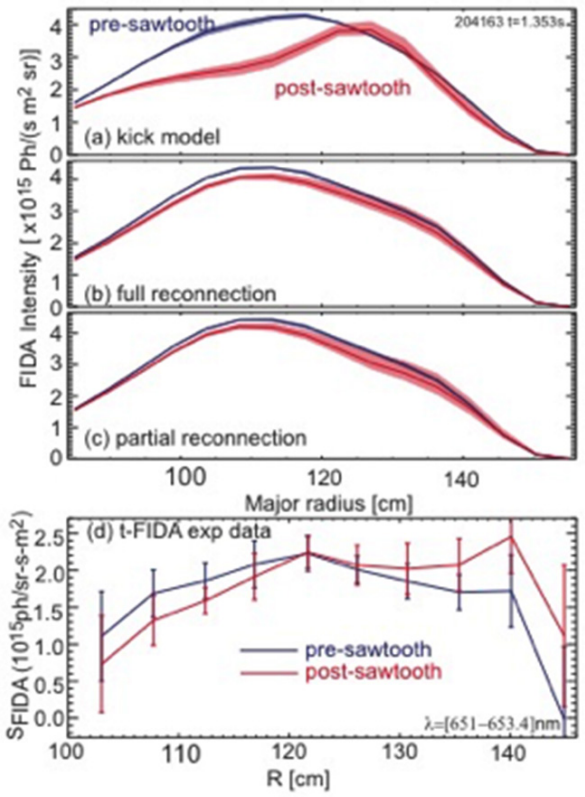

Figure 8. Comparison of t-FIDA spatial profiles calculated by the FIDASIM [32] synthetic diagnostic code using the plasma profiles and fast ion distribution from (*a*) the kick model, (*b*) the Kadomstev full reconnection model, and (*c*) the Porcelli partial reconnection model. The measured t-FIDA profiles are shown in (*d*). Reprinted from [31].

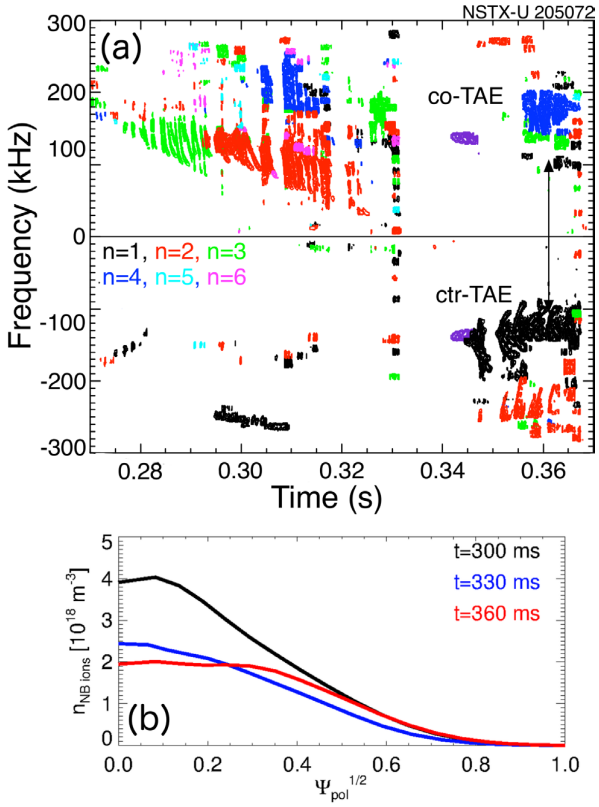

Figure 9. (*a*) Toroidal mode number spectrum for co- and counter-propagating TAEs. Counter-TAEs occur when one of the more outboard pointing beamlines turns on. (*b*) Fast ion density profile at three different times from TRANSP/NUBEAM. Adapted courtesy of IAEA. Figure from [37]. Copyright 2018 IAEA.

sawtooth induced fast ion redistribution may be required. The particle-following code ORBIT has been used to characterize the redistribution of fast particles as a function of their parameters such as energy, pitch, and radial location. Due to a sawtooth crash, as expected, the redistribution of fast ions in real space shows that fast particles with different orbit types are affected differently by the sawtooth instability, as observed in experiments. Initial interpretative TRANSP simulations using the kick model based on the ORBIT modeling results show features in the fast ion redistribution before/after a sawtooth crash that resemble the experimental data, as shown in figure 8 [30, 31]. With the fast ion distribution from the kick model, the simulated t-FIDA spatial profile qualitatively reproduces the t-FIDA observations especially the increase near the edge (figures 8(*a*) and (*d*)). Those features cannot be reproduced by either full or partial reconnection models (figures 8(*b*) and (*c*)).

4.2. Counter-propagating toriodal Alfvén eigenmodes (TAEs) full phase space effects

A broad NBI deposition profile is usually thought to reduce the drive for Alfvénic instabilities by reducing the radial gradient of the EP density. However, NSTX-U scenarios with off-axis NBI show evidence that broad profiles associated with tangential and off-axis neutral beam injection could lead to the destabilization of Alfvénic instabilities. An example is given in figure 9, showing the spectrum that includes both co- and counter-current propagating TAE modes. Theory predicts the destabilization of counter-TAEs for hollow EP density profiles [33]. However, for this case counter-TAEs are observed at times for which TRANSP/NUBEAM[22] predict a peaked or flat EP density profiles.

TAE stability was investigated in TRANSP through the reduced 'kick' model [34, 35]. Potentially unstable eigenmodes are first identified via the NOVA-K code [36]. The EP response to each mode is then investigated through the orbit-following code ORBIT. The results are combined to form a transport probability matrix, used in the NUBEAM module of TRANSP to introduce enhanced EP transport by the instabilities and to infer mode stability [34].

Results of TAE stability analysis at two different times are shown in figure 10. The predicted unstable spectrum of TAEs is in reasonable agreement with the experimental observations, including a transition from co-TAEs only at earlier times to co- and counter-TAEs after $t = 340$ ms. Furthermore, the TRANSP and kick model analysis indicates that instabilities are driven by a combination of both radial and energy gradients in the EP distribution function [37]. The mechanisms for wave-particle interaction revealed by the energetic particle

[22] TRANSP (https://doi.org/10.11578/dc.20180627.4)

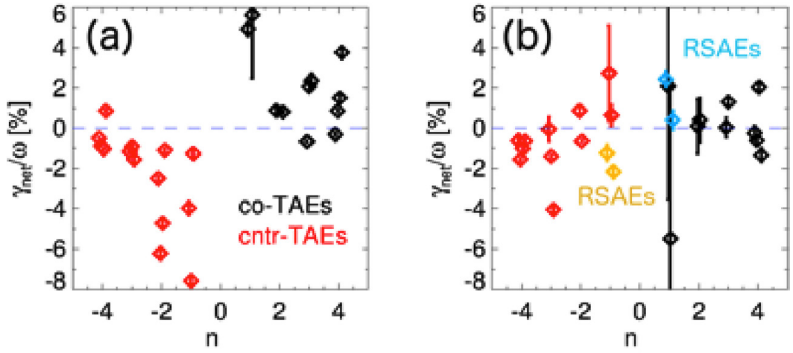

Figure 10. Net growth rate (including damping rate from NOVA-K) for co- and counter-propagating TAEs at two different times, 340 ms (*a*) and 365 ms (*b*). The analysis recovers the transition from co-TAEs only to co- plus counter-TAEs after $t = 340$ ms, see figure 9. The predicted unstable spectrum is consistent with the experimental observations. Reproduced courtesy of IAEA. Figure from [37]. Copyright 2018 IAEA.

phase space resolved analysis are the starting point to identify strategies to mitigate or suppress the observed instabilities, e.g. by varying the injected NBI mix to populate EP phase space regions where wave-particle resonant interactions are reduced.

4.3. Role of microturbulence in TAE chirping

The spectral characteristics of Alfvén eigenmodes (AEs), such as reversed shear and toroidal AEs (RSAEs and TAEs), in tokamaks can vary considerably, depending on several parameters affecting their resonant interaction with fast ions [38]. When the resonant ions experience considerable scattering (e.g. from Coulomb collisions, overlap with other modes, RF heating, turbulence and 3D fields), they are only able to remain within the phase-space resonance island for a limited time before being detuned from it. This implies that the fast ion dynamics are dominated by the cumulative effect of several kicks due to different resonances and therefore should lead to a diffusive type of losses. However, when the ions can remain resonating coherently for several wave trapping (or bounce) times, the wave can evolve towards self-organizing responses, e.g. when the resonance condition changes on a sub-millisecond timescale, allowing the wave to compensate background damping losses by accessing the gradient of the distribution function over the extended range in phase space. This scenario is associated with wave chirping and avalanching of several modes, leading to convective losses of fast ions.

The ability to predict, for a given plasma background, what the nature of Alfvénic oscillation (fixed-frequency, leading to diffusive losses, or chirping/avalanching, leading to convective losses) will be of considerable advantage for measures aiming at the mitigation of fast ion transport [38]. For example, for the case of dominant diffusive losses, reduced modeling such as a resonance broadened quasilinear theory, is expected to be sufficient to capture the essence of the self-consistent evolution of the fast ion distribution function [39, 40].

Spherical tokamaks tend to exhibit Alfvénic chirping and avalanching, accompanied by wave amplitude bursting [41], while conventional tokamaks tend to have Alfvénic waves oscillating with a nearly fixed frequency and a quasi-steady amplitude. To be able to explain this observation, a criterion for the likelihood of chirping oscillations was developed based on previous analytical works on the theory of driven, kinetic instabilities near threshold with dissipation [42–44] and evaluated for a number of NSTX, DIII-D and TFTR discharges [45–47] using the stability code NOVA-K. The work predicted, and verified experimentally, that micro-turbulence can be a strong mediator between the mode transition from fixed-frequency to chirping and vice-versa. In spherical tokamaks, particles spend more time in the good curvature region and experience higher relative rotation shear. Therefore, STs naturally exhibit lower anomalous transport due to microturbulence with respect to conventional tokamaks. For example, on NSTX the total thermal ion diffusivity has been found to be of order of its neoclassical level [48]. These distinct turbulence features have been found to explain why chirping instabilities are rare in conventional tokamaks and common in spherical tokamaks since the turbulence acts to effectively increase the scattering experienced by the resonant fast ions [49] and therefore to prevent the chirping and avalanching responses.

In order to improve the evaluation of the criterion for chirping onset, NSTX discharges that show toroidicity-induced Alfvén waves transitioning from constant frequency to chirping have been analyzed with the gyrokinetic code GTS. The δf particle-in-cell nonlinear electrostatic ion temperature gradient and trapped electron mode simulations included fully kinetic electrons and plasma profiles which were input from TRANSP. The global simulations covered a range in the normalized square root of the toroidal flux from 0.2 to 0.8. The simulation results, shown in figure 11 support the theoretical prediction that a marked decrease in turbulence-driven EP transport causes the onset of chirping.

Predictions for baseline ELMy, reversed-shear and hybrid scenarios of ITER planned experiment have also been recently explored [50] and shown to be near the borderline between the fixed-frequency and the chirping regimes when collisional and microturbulent effects are accounted for. For scenarios in which other resonance decorrelating mechanisms are important, the toroidal and reversed shear Alfvénic modes would then be expected to exhibit a steady response with no frequency excursion.

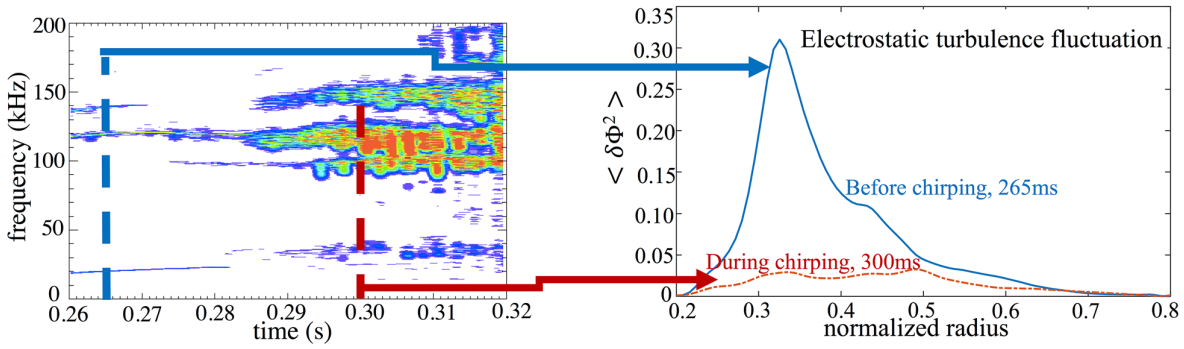

Figure 11. Correlation between mode transition from fixed-frequency to chirping spectral response (left) and a marked drop of the electrostatic turbulent potential calculated by GTS (right), for NSTX shots 135388. Reproduced courtesy of IAEA. Figure from [50]. Copyright 2018 IAEA.

4.4. Global Alfvén eigenmode (GAE) suppression by off-axis neutral beam injection

Multiple GAEs with a range of toroidal mode numbers and frequencies are commonly observed in beam-heated NSTX plasmas. The GAEs propagate counter to the tangentially injected beam ions and are excited through an ion cyclotron resonance with the co-moving beam ions. The GAE frequencies are down-shifted from the ion cyclotron frequency by the motion of the beam ions; that is, in the moving frame of the beam ions, the GAE frequency is up-shifted to the ion-cyclotron frequency. In NSTX-U it has been experimentally demonstrated that this ubiquitous mode can be completely suppressed with the judicious injection of a relatively small amount of fast ions injected nearly parallel to the magnetic field, i.e. $v_{\|}/v \approx 1$. An analytic theory describing the Doppler-shifted ion cyclotron resonance (DCR) drive for the GAE [51], as well as numerical modeling, have been used to very successfully describe this suppression technique [52]. The simple analytic model of the DCR GAE stability can be used to predict the scaling of the GAE frequencies and toroidal mode numbers [53]. In figure 12, the predictions of this simple model for the scaling of frequency and toroidal mode number are compared with experimental results. Here the mode frequency drops and the toroidal mode numbers increase in time as the plasma density increases and the $q(0)$ drops.

The GAE mode was completely suppressed after $t = 0.45$ s with the injection of fast ions nearly parallel to the magnetic field, i.e. $V_{\|}/V \approx 1$, from the new, tangential neutral beam on NSTX-U [53]. HYM simulations have been used to reproduce the experimental findings [54, 55]; before additional beam injection the simulations show unstable counter-rotating GAEs with toroidal mode numbers $n = -7$ to -11, and frequencies that match the experimentally observed unstable GAEs (figure 13). The calculated growth rates (figure 13 top) for the most unstable GAEs with $n = -10$ and -11 are about two to three times higher than that estimated from the experimental data, probably due to an underestimated damping by the bulk plasma MHD model. Nonlinear simulations show the peak saturation amplitudes of $\delta B/B_0 \sim 1$ to 5×10^{-3}, comparable to experimental estimates ($\delta B/B_0 \sim 2.7 \times 10^{-3}$ for the $n = -10$ and $\delta B/B_0 \sim 1.8 \times 10^{-3}$ for the $n = -11$ modes).

HYM simulations also show that off-axis neutral beam injection strongly suppresses all unstable GAEs even for a relatively weak added beam. In simulations the fraction of the off-axis beam population of the total beam ion inventory has been varied from 4.3% to 17%. Figure 14 shows the growth rate of the $n = -11$ GAE versus $N_{\mathrm{add}}/N_{\mathrm{tot}}$ parameter, which is the fraction of the beam ion population that is from the off-axis midplane neutral beam. Simulations found that the unstable $n = -11$ GAE is stabilized when fraction of the additional beam ions is larger than 7%. The stabilization threshold is lower for lower $|\, n \,|$ unstable modes. This is consistent with the experimental observation that the GAEs become suppressed at the point where the neutron rate had increased by 6%, a rough experimental indication that the fast ion population has also increased by 6%, as the neutrons are predominantly from beam-target reactions.

In NSTX, cases were found where high harmonic fast wave heating also suppressed fully the GAE modes [56].

4.5. Energetic particle-modified modes

Spherical tokamaks like NSTX/NSTX-U routinely operate with super-Alfvénic beam ions, and the concomitant broad spectrum of fast-ion driven instabilities. Fully self-consistent hybrid MHD/particle simulations reveal strong energetic particle modifications to sub-cyclotron GAEs in low-aspect ratio, NSTX-like conditions [57]. Linear simulations were run with HYM [54, 55], an initial value code in full 3D toroidal geometry in which a single-fluid thermal plasma is coupled to full orbit kinetic fast ions. The equilibrium is solved self-consistently with the inclusion of fast ions, which can carry current comparable to that of the thermal plasma.

In this set of simulations, key parameters defining the beam-like fast ion distribution function, such as the normalized injection velocity and central pitch, were varied in order to study their influence on the characteristics of the excited modes [57]. The fast ion distribution was modeled as a slowing-down function in energy and Gaussian in pitch. It was found that the frequency of the most unstable mode for each toroidal harmonic changes significantly and continuously with beam parameters, depending most substantially on the injection velocity, as shown in figure 15. This result is present for both co- and counter-propagating GAEs, where the linear dependence and sign of

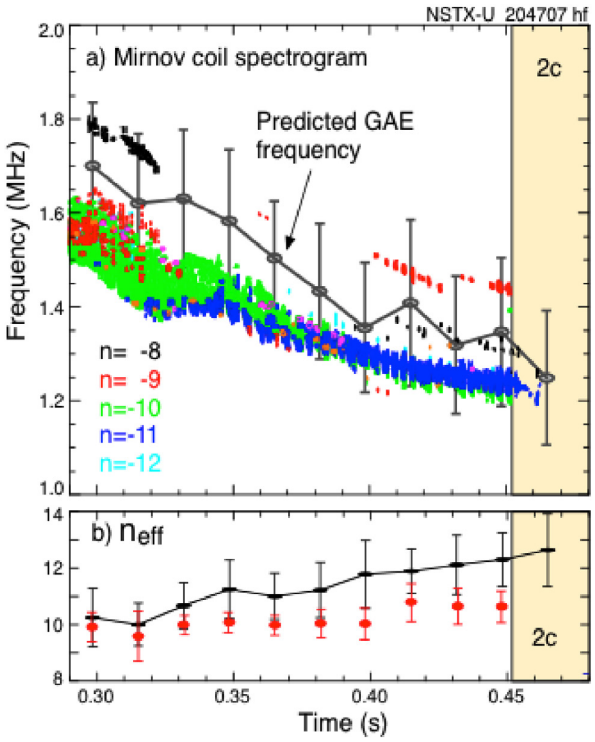

Figure 12. (*a*) Color-coded spectrogram showing ctr-propagating GAE activity. Dominant modes evolve from $n = -9$ (red) and $n = -10$ (green) to $n = -10$ and $n = -11$ (blue), the grey curve is the predicted GAE frequency evolution. (*b*) Predicted GAE mode number evolution, red is experiment, black the model predictions. Adapted courtesy of IAEA. Figure from [53]. Copyright 2018 IAEA.

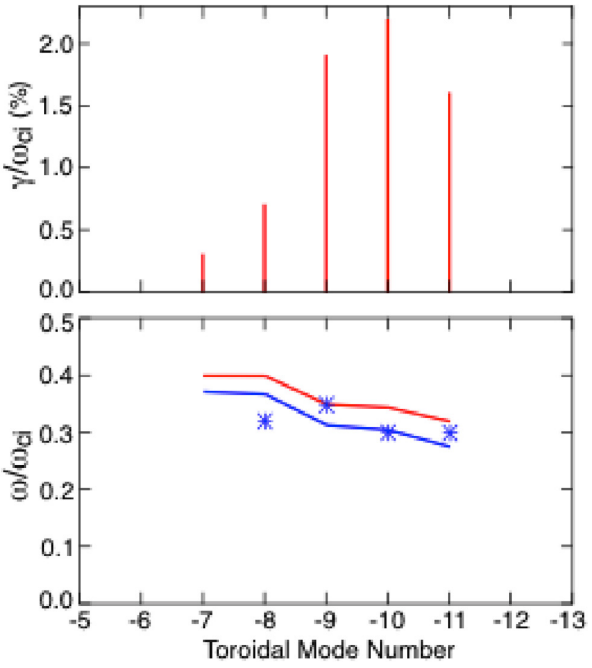

Figure 13. Growth rates and frequencies of unstable counter-GAEs from simulations as function of toroidal mode number. The blue line is Doppler-shift corrected frequencies; the star symbols are experimental values. Adapted figure with permission from [52], Copyright 2017 by the American Physical Society.

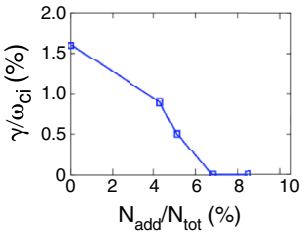

Figure 14. Growth rate of the $n = -11$ GAE as a function of fraction of beam ion population that is from the off-axis midplane neutral beam.

the change are consistent with the Doppler-shifted cyclotron resonances, which drive the modes. There are no clear concurrent changes in mode structure (i.e. changes in poloidal or radial mode numbers) that would indicate that these frequencies correspond to distinct eigenmodes, especially for co-GAEs.

Varying the fast ion density between simulations confirmed that the mode frequency is sensitive to equilibrium changes due to energetic particle effects; however, it was found that equilibrium changes themselves were an order of magnitude too small to account for the frequency dependence on injection velocity. Additional simulations conducted with a fixed MHD equilibrium (excluding the fast ion contributions from the equilibrium) and varying injection velocity reproduced nearly all of the change in frequency, demonstrating that the location of fast ions in phase space plays a more vital role in determining the frequency of the most unstable mode than their modification of the equilibrium does.

The key takeaway is that if the resonant parallel velocity of particles driving the mode is proportional to the beam injection velocity, then the large frequency changes are understood as a consequence of the resonance condition. This is plausibly based on a perturbative GAE growth rate expression, derived by Gorelenkov *et al* [51] and adapted to the cases studied here, which yields a growth rate depending on the injection velocity and parallel resonant velocity. Numerical evaluation reveals that the growth rate is maximized when the parallel resonant velocity is a fixed fraction of the injection velocity, independent of the injection velocity, as shown in figure 16. Furthermore, this critical value is robust to changes in other parameters in the growth rate expression for a wide range of relevant values. This calculation suggests a linear relationship between the injection velocity and parallel resonant velocity, which combined with the resonance condition may explain why the frequency of the most unstable mode depends so dramatically on the injection velocity.

An energetic particle mode (EPM) defined by a continuum of $k_{||}$ values to choose from as the injection velocity is varied is consistent with these findings, and could indicate the existence of a new EPM, referred to here as an energetic-particle-modified GAE (EP-GAE). This may be the first instance of an EPM driven by the cyclotron resonance and excited at an appreciable fraction of the cyclotron frequency instead of near EP orbital frequencies. Moreover, these simulations demonstrate that the nonperturbative regime for these modes was

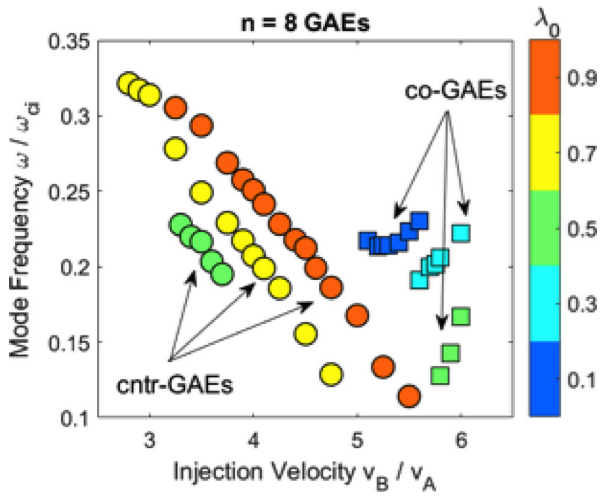

Figure 15. Change in frequency for $|n| = 8$ GAEs as a function of the normalized beam injection velocity. Counter-GAEs are marked by circles, co-GAEs by squares. Color denotes the central pitch, $\lambda_0 = \mu B_0/\epsilon$, of the beam distribution in each simulation. On-axis cyclotron frequency is 2.4 MHz. Reprinted from [57], with the permission of AIP Publishing.

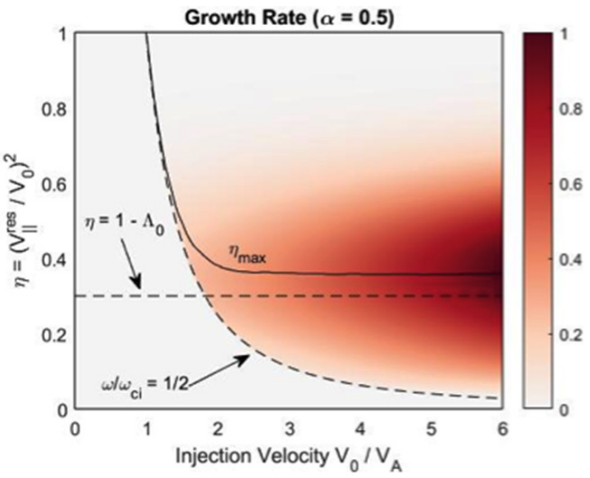

Figure 16. Fast ion drive (color) as a function of injection velocity and resonant parallel velocity fraction of the injection velocity. The dashed curve shows the $\omega/\omega_{ci} \leqslant 1/2$ boundary where the calculation is valid. The dashed horizontal line is a sufficient but no necessary condition for net fast ion drive. The solid curve shows the resonant parallel velocity fraction that maximizes the growth rate for each value of injection velocity. The fast ion drive is in arbitrary units. Reprinted from [57], with the permission of AIP Publishing.

routinely accessed in NSTX operating conditions. The basic picture of an energetic beam driving an MHD mode of the thermal plasma without modifying its attributes is seen to break down in conditions where the beam pressure is comparable to the thermal plasma pressure. This may have implications for the ongoing investigation into the anomalously flat electron temperature profiles observed in NSTX at high beam power, which are correlated with substantial high frequency Alfvénic activity [58, 59]. Prospects for future experimental verification of the EP-GAE are promising, as its defining characteristics should be observable in suitably designed experiments on NSTX-U.

5. Edge and divertor physics

5.1. Scrape-off layer (SOL) turbulence

Understanding edge turbulence is important since it affects plasma transport across the edge, and so controls to some extent the width of the high heat flux region at the divertor plate. A higher level of turbulent transport in the edge is beneficial for reducing the peak heat load at the divertor plate. Gas puff imaging [60] was used to characterize edge and SOL turbulence in NSTX. This turbulence can be mathematically described by a two-dimensional cross-correlation function, which measures its spatial structure perpendicular to the magnetic field. New results, analyzing in great detail the two-dimensional turbulence cross-correlation functions in the edge of NSTX, were published [61]. Figure 17(*a*), shows a rather complex pattern in which the correlation function varies with the radial location in the plasma (varying from left-to-right from 6 cm inside the separatrix to 6 cm outside the separatrix), The patterns showed both negative and positive correlation structures, depending on the choice of reference location. These are among the most detailed measurements of this kind ever made in a tokamak.

Recent theoretical work [62] has attempted to explain these observations within the paradigm of blob–hole pair dynamics, in which blobs contain higher pressure and density than the surrounding plasma, and holes lower pressure and density. 1D and 2D correlations were determined from the theory results and compared directly to experiment. The semi-analytic model used for this study qualitatively reproduced a number of the experimental observations. For instance, the model reproduced the dipole-like structures whose correlations flipped in sign depending on reference point position. Further, the 2D spatial correlation patterns determined from the model were similar to those that were measured (figure 17(*b*)). However, while the 2D correlations from theory showed the blob regions moving outward in time and the hole regions moving inward, the 2D correlations from experimental data showed only the former. When the experimental data maximum and minimum turbulence points (which are more sensitive and localized than the more averaged 2D spatial correlations) were tracked, both the blob and the hole motion expected from theory were reproduced on average. Future work will address how these results relate to results of XGC1 [63] calculations, which predict a significant broadening of the SOL heat flux width due to turbulence for 2 MA NSTX-U discharges [64].

5.2. Divertor-localized turbulence

The characterization of the structure of SOL/divertor turbulence is critical to interpret divertor measurements and transport and to understand divertor heat fluxes in present tokamaks and in ITER, where a narrow heat flux width could challenge wall

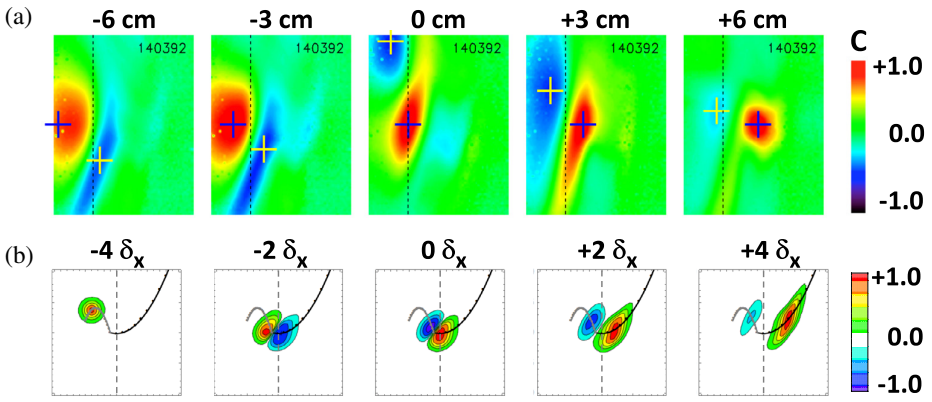

Figure 17. (*a*) Experimental 2D spatial correlation patterns, with the correlation reference location varying from −6 cm inside the separatrix to 6 cm outside. (*b*) 2D spatial correlations as determined from simple blob theory [62]. Here, the spatial scales are normalized to the blob size, δ_x, (Gaussian half-width in the radial direction) and successive frames, left to right, correspond to different correlation reference locations relative to the nominal separatrix at $x = 0$ (dashed line), as indicated by the labels $-4\delta_x$ to $+4\delta_x$. The shifts are chosen to be similar to those in (*a*). The theory shows a similar relation between the positive and negative correlation regions as a function of correlation reference location. Adapted from [62].

materials. Recent work in NSTX-U led to the observation of divertor leg turbulence, where divertor leg indicates the region below the X-point radially limited to a few centimeters around the separatrix [65]. Filamentary fluctuations localized on the divertor legs were observed in NSTX-U L-mode discharges via fast camera imaging. The typical structure of divertor filaments is shown in figure 18(*a*) with a rendering of flux tubes in the NSTX-U divertor corresponding to divertor localized fluctuations, and in figure 18(*b*) with an image of the lower divertor with 9 μs exposure, showing filaments on the inner and outer divertor legs. Filaments were approximately field aligned, connected to the divertor target plate and localized to the bad curvature region on both the inner (i.e. in the private flux region) and the outer divertor legs (i.e. in the common flux region). Spatial separation (radially) between divertor leg modes and divertor turbulence due to upstream blobs was confirmed by their intersection on the divertor target plate, indicating the limited penetration of upstream modes near the separatrix. Characteristic frequencies were 10–30 kHz with filament lifetimes of 50–100 μs and near-Gaussian probability density functions on both divertor legs. Poloidal and radial correlation lengths on the divertor legs were comparable and on the order of 10–100 ion gyroradii (1–4 cm), suggesting the local generation of these filaments. Parallel correlation lengths were ∼2–3 m on both divertor legs, corresponding to more than a toroidal turn for inner leg filaments and about half of a toroidal turn for outer leg filaments. No correlation was observed with midplane turbulence. The limited parallel correlation length of both inner and outer leg turbulence can be indicative of the role of X-point disconnection.

The filament localization to the bad curvature side of divertor legs and the absence of correlation with midplane turbulence and between inner and outer legs motivated simulations performed with the ArbiTER (arbitrary topology equation reader) code [66] with a simulation grid limited to the divertor legs (between X-point and divertor target plate), separately for the inner and outer leg. Background

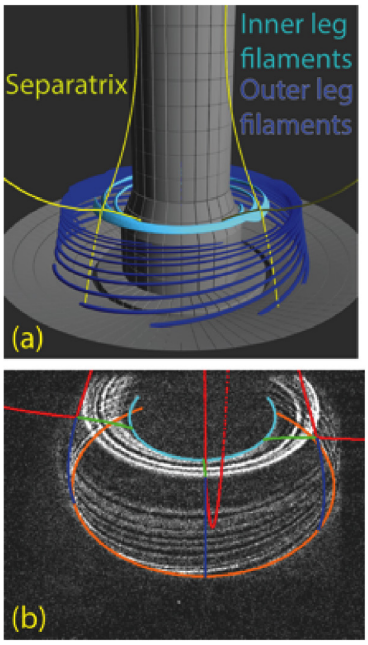

Figure 18. (*a*) Rendering of the NSTX-U divertor with flux tubes corresponding to divertor-localized fluctuations. (*b*) Divertor image in C III emission (9 μs exposure) after high pass filtering. Separatrix (red), inner (green) and outer (blue) divertor legs, inner (cyan) and outer (orange) strike points are overlaid. Reproduced courtesy of IAEA. Figure from [65].

profiles were derived from UEDGE simulations constrained by midplane experimental profiles. In both divertor legs, instabilities localized to the bad curvature side of the leg were identified and were driven by the interaction of density gradients with geodesic curvature. Outer leg modes showed growth rate saturation for higher mode numbers than inner leg modes, in qualitative consistence with experimental observations.

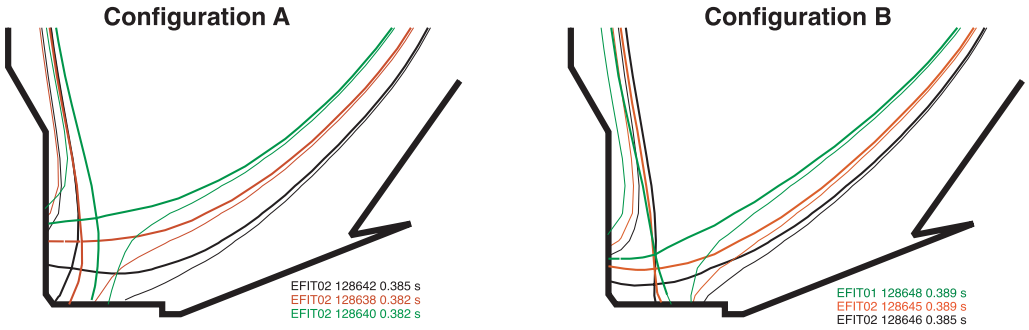

Configuration	Coils	X-pt height (m)	R OSP (m)	Separatrix poloidal angle with target at OSP (deg.)
A	PF1AL	0.088-0.182	0.297-0.394	51-68
B	PF1AL & PF1B	0.049-0.125	0.399-0.431	99-105

Figure 19. Two divertor configurations studied in NSTX. $\alpha \leqslant 90°$ in Configuration A, while $\alpha > 90°$ in Configuration B, where α is the angle at which magnetic field lines hit the lower divertor plate.

5.3. Divertor detachment optimization

New analysis of divertor geometry effects in NSTX demonstrated that highly shaped ST plasmas (with naturally high elongation and triangularity) have several favorable effects for dissipative divertor optimization. The inherently high poloidal flux expansion (leading to reduced peak divertor heat flux), as well as plasma plugging and higher recycling (leading to lower divertor temperature and higher divertor density) help mitigate the unfavorable effect created by the open horizontal plate divertor configuration. These configurations are naturally created in NSTX and NSTX-U with the existing (and planned) divertor coil layout.

The NSTX experiment compared several standard lower single null divertor geometries differing by the outer divertor leg orientation and poloidal length with respect to the divertor plate [67]. Figure 19 shows the configurations compared. The divertor poloidal leg length variation resulted in several effects: a longer parallel connection length (hence more parallel/perpendicular dissipation and different parallel temperature gradients), higher degree of divertor plasma plugging efficiency (hence higher divertor neutral compression at lower X-point height), and higher poloidal flux expansion (resulting in reduced deposited peak heat flux). The divertor poloidal leg orientation is described by α, which is the poloidal angle at which magnetic field lines hit the lower divertor plate. The configurations with $\alpha \leqslant 90°$ (Configuration A) directed the recycling neutral flux toward the separatrix, led to enhanced recycling and higher neutral pressure (the vertical target plate effect). In other configurations with $\alpha > 90°$ (Configuration B), the neutrals were recycled toward the outer SOL and contributed less to ionization in the divertor. Re-ionization of recycling neutrals in the divertor chamber termed flux amplification is an essential feature of the high-recycling divertor regime. As the recycling is increased, the divertor density increased, the divertor temperature further decreased, leading to increased dissipation (i.e. higher P_{rad} and momentum loss), loss of parallel pressure balance, and a transition to detachment. The experimental scans were compared to two models: the two-dimensional multi-fluid plasma model with charge state resolved carbon impurity implemented in the UEDGE code, and a reduced heat flux model used for divertor heat flux modeling is NSTX-U plasma facing component engineering design. Both models provided support to the hypothesis that the highly shaped ST plasmas inherently create divertor configurations with a higher degree of dissipation (as might be compared to divertor configurations in weakly shaped plasmas).

6. NSTX-U recovery plans and status

The NSTX-U recovery planning is ongoing, with numerous design improvements included in order to support flexible operations and increase reliability to achieve key mission goals. New requirements for the divertor heat fluxes have been defined, based on recent SOL heat flux width models. New halo currents loads have been determined based on combining data from NSTX, NSTX-U, MAST, and conventional aspect ratio devices. New error field analysis has been conducted, with the goal of optimizing both the global MHD stability and minimizing plasma-facing component heat flux asymmetries for scenarios with large poloidal flux expansion. New designs of graphite plasma facing components utilize castellations to reduce the mechanical stresses, allowing tiles to reach surface temperature limits, $\sim$1600 °C. Improved divertor coil designs simplify fabrication and facilitate turn-to-turn testing. Modifications to the NSTX-U vacuum chamber to increase system reliability will eliminate one of the ceramic insulators necessary for coaxial helicity injection. NSTX-U is expected to resume operations in 2021.

7. Conclusions

A great deal of analysis and modeling of both NSTX and NSTX-U data, covering a number of areas of tokamak physics research, has been accomplished over the past two years during the NSTX-U recovery outage. The work has focused on coupling experiment and theory with the goal of understanding underlying physical processes and the development of reliable and robust predictive models through experimental validation of developing theory. These predictive models will provide a basis for assessing the potential of the low aspect ratio, or spherical, configuration as a possible approach for a compact pilot plant.

Gyrokinetic analyses have identified the potential importance of multi-scale effects for understanding coupled turbulence and transport processes and for being able to predict plasma temperature profiles accurately at low aspect ratio. Low aspect ratio effects have been key to understanding differences in neoclassical tearing mode growth and structures between low and higher aspect ratio, and non-linear simulations of vertical disruption events allow for realistic predictions of disruption time scale and forces on the plasma-facing components and vacuum vessel. Energetic particle studies cover a wide range of wave-particle interactions across a wide frequency range that result in fast ion redistribution and loss. These studies, however, also identify mechanisms that can be used to mitigate and even suppress the fast-ion-driven instabilities, either through plasma microturbulence or through phase space engineering of the fast ion population. The studies have also resulted in the development of models that are moving towards being fully predictive, which will be used in developing high performance scenarios in future devices. Finally, studies of edge turbulence in the main chamber as well as the divertor region, and their coupling, give insights into the processes controlling heat flux profiles and magnitudes, which is essential for designing the materials at the plasma interface. NSTX-U recovery activities are ongoing with numerous design improvements to provide more flexible and robust operation of NSTX-U, which is expected to resume in 2021.

Acknowledgments

This manuscript is based upon work supported by the US Department of Energy, Office of Science, Office of Fusion Energy Sciences, and has been authored by Princeton University under Contract Number DE-AC02-09CH11466 and Lawrence Livermore National Laboratory under Contract Number DE-FG02-02ER54678 with the US Department of Energy. The publisher, by accepting the article for publication, acknowledges that the United States Government retains a non-exclusive, paid-up, irrevocable, world-wide license to publish or reproduce the published form of this manuscript, or allow others to do so, for United States Government purposes.

ORCID iDs

D.J. Battaglia https://orcid.org/0000-0001-8897-9740
V.N. Duarte https://orcid.org/0000-0001-8096-7518
W. Guttenfelder https://orcid.org/0000-0001-8181-058X

References

[1] Menard J.E. *et al* 2012 *Nucl. Fusion* **52** 083015
[2] Menard J.E. *et al* 2011 *Nucl. Fusion* **51** 103014
[3] Menard J.E. *et al* 2016 *Nucl. Fusion* **56** 106023
[4] Menard J.E. 2019 *Phil. Trans. R. Soc.* A **377** 20170440
[5] Menard J.E. *et al* 2017 *Nucl. Fusion* **57** 102006
[6] Battaglia D.J. *et al* 2018 *Nucl. Fusion* **58** 046010
[7] Howard N. *et al* 2016 *Phys. Plasmas* **23** 056109
[8] Holland C. *et al* 2017 *Nucl. Fusion* **57** 066043
[9] Staebler G.M. *et al* 2017 *Nucl. Fusion* **57** 066046
[10] Ren Y. *et al* 2013 *Nucl. Fusion* **53** 083007
[11] Wang W. *et al* 2006 *Phys. Plasmas* **13** 092505
[12] Wang W. *et al* 2015 *Phys. Plasmas* **22** 102509
[13] Guttenfelder W. *et al* 2011 *Phys. Rev. Lett.* **106** 155004
[14] Ren Y. *et al* 2012 *Phys. Plasmas* **19** 056125
[15] Staebler G.M. *et al* 2016 *Phys. Plasmas* **23** 062518
[16] Guttenfelder W. *et al* 2019 *Nucl. Fusion* **59** 056027
[17] Ruiz Ruiz J. *et al* 2015 *Phys. Plasmas* **22** 122501
[18] Maingi R. *et al* 2010 *Phys. Rev. Lett.* **105** 135004
[19] Menard J.E. *et al* 2005 *Nucl. Fusion* **45** 539
[20] Gerhardt S.P. *et al* 2009 *Nucl. Fusion* **51** 033004
[21] Gerhardt S.P. *et al* 2011 *Nucl. Fusion* **49** 032003
[22] La Haye R.J. and Sauter O. 1998 *Nucl. Fusion* **38** 987
[23] La Haye R.J. 2006 *Phys. Plasmas* **13** 055501
[24] Ferraro N., Jardin S.C. and Snyder P.B. 2010 *Phys. Plasmas* **17** 102508
[25] Hegan C. 1999 *Phys. Plasmas* **6** 3980
[26] Berkery J.W. *et al* 2017 *Phys. Plasmas* **24** 056103
[27] Sabbagh S.A. *et al* 2018 Disruption event characterization, forecasting in tokamaks *Preprint: 2018 IAEA Fusion Energy Conf.* (*Gandhinagar, India*, *22–27 October 2018*) EX/P6-26
[28] Pfefferlé N. *et al* 2018 *Phys. Plasmas* **25** 056106
[29] Liu D. *et al* 2018 *Nucl. Fusion* **58** 082028
[30] Kim D. *et al* 2018 *Nucl. Fusion* **58** 082029
[31] Kim D. *et al* 2019 Investigation of fast particle redistribution induced by sawtooth instability on NSTX-U *Nucl. Fusion* accepted (https://doi.org/10.1088/1741-4326/ab1f20)
[32] Heidbrink W.W. *et al* 2011 *Commun. Comput. Phys.* **10** 716
[33] Wong H.V. and Berk H.L. 1999 *Phys. Lett.* A **251** 126
[34] Podestà M., Gorelenkova M. and White R.B. 2014 *Plasma Phys. Control. Fusion* **56** 055003
[35] Podestà M., Gorelenkova M. and Gorelenkov N.N. 2017 *Plasma Phys. Control. Fusion* **59** 095008
[36] Cheng C. 1992 *Phys. Rep.* **211** 1
[37] Podestà M., Fredrickson E.D. and Gorelenkova M. 2018 *Nucl. Fusion* **58** 082023
[38] Gorelenkov N.N., Pinches S.D. and Toi K. 2014 *Nucl. Fusion* **54** 125001
[39] Berk H.L. *et al* 1995 *Nucl. Fusion* **35** 1661
[40] Gorelenkov N.N., Duarte V.N., Podesta M. and Berk H.L. 2018 *Nucl. Fusion* **58** 082016
[41] McClements K.G. and Fredrickson E.D. 2017 *Plasma Phys. Control. Fusion* **59** 053001
[42] Berk H.L., Breizman B.N. and Pekker M. 1996 *Phys. Rev. Lett.* **76** 1256
[43] Berk H.L., Breizman B.N. and Pekker M. 1997 *Plasma Phys. Rep.* **23** 778
[44] Lilley M.K., Breizman B.N. and Sharapov S.E. 2009 *Phys. Rev. Lett.* **102** 195003
[45] Duarte V.N. *et al* 2017 *Nucl. Fusion* **57** 054001
[46] Duarte V.N. *et al* 2017 *Phys. Plasmas* **24** 122508
[47] Berk H.L. *et al* 2016 Chirping in plasmas; test of criterion for chirping onset, simulation of explosive chirping *Preprint: 2016 IAEA Fusion Energy Conf. (Kyoto, Japan*, *17–22 October 2016)* PDP-10
[48] Kaye S.M. *et al* 2007 *Nucl. Fusion* **47** 499
[49] Lang J. and Fu G.-Y. 2011 *Phys. Plasmas* **18** 055902

[50] Duarte V.N. *et al* 2018 *Nucl. Fusion* **58** 092013
[51] Gorelenkov N.N. *et al* 2003 *Nucl. Fusion* **43** 228
[52] Fredrickson E.D. *et al* 2017 *Phys. Rev. Lett.* **118** 265001
[53] Fredrickson E.D. *et al* 2018 *Nucl. Fusion* **58** 082022
[54] Belova E.V. *et al* 2000 *Phys. Plasmas* **7** 4996
[55] Belova E.V., Gorelenkov N.N. and Cheng C.Z. 2003 *Phys. Plasmas* **10** 3240
[56] Fredrickson E.D. *et al* 2015 *Nucl. Fusion* **55** 013012
[57] Lestz J.B., Belova E.V. and Gorelenkov N.N. 2018 *Phys. Plasmas* **25** 042508
[58] Stutman D. *et al* 2009 *Phys. Rev. Lett.* **102** 115002
[59] Ren Y. *et al* 2017 *Nucl. Fusion* **57** 072002
[60] Zweben S.J. *et al* 2015 *Nucl. Fusion* **55** 093035
[61] Zweben S.J. *et al* 2017 *Phys. Plasmas* **24** 102509
[62] Myra J.R., Zweben S.J. and Russell D.A. 2018 *Plasma Phys. Control. Fusion* **60** 075015
[63] Ku S., Chang C.S. and Diamond P.H. 2009 *Nucl. Fusion* **49** 115021
[64] Chang C.S. 2018 private communication
[65] Scotti F. *et al* 2018 *Nucl. Fusion* **58** 126028
[66] Baver D., Myra J.R. and Umansky M.V. 2018 *Commun. Comput. Phys.* **20** 136
[67] Soukhanovskii V. 2019 Divertor detachment optimization in an unfavorable open geometry horizontal target divertor configuration in NSTX and NSTX-U *Int. Conf. on Plasma Surface Interactions in Controlled Fusion Devices (Princeton, NJ, 17–22 June 2018)* (https://psi2018.princeton.edu)